Title
Siderocalin-mediated recognition, sensitization, and cellular uptake of actinides

Journal
Proceedings of the National Academy of Sciences of the United States of America, 112(33)

ISSN
0027-8424

Authors
Allred, Benjamin E
Rupert, Peter B
Gauny, Stacey S
et al.

Publication Date
2015-08-18

DOI
10.1073/pnas.1508902112

Peer reviewed

Siderocalin-mediated recognition, sensitization, and cellular uptake of actinides

Benjamin E. Allred[a], Peter B. Rupert[b], Stacey S. Gauny[a], Dahlia D. An[a], Corie Y. Ralston[c], Manuel Sturzbecher-Hoehne[a], Roland K. Strong[b], and Rebecca J. Abergel[a,1]

[a]Chemical Sciences Division, Lawrence Berkeley National Laboratory, Berkeley, CA 94720; [b]Division of Basic Sciences, Fred Hutchinson Cancer Research Center, Seattle, WA 98109; and [c]Berkeley Center for Structural Biology, Lawrence Berkeley National Laboratory, Berkeley, CA 94720

Edited by Tobin J. Marks, Northwestern University, Evanston, IL, and approved July 15, 2015 (received for review May 6, 2015)

Synthetic radionuclides, such as the transuranic actinides plutonium, americium, and curium, present severe health threats as contaminants, and understanding the scope of the biochemical interactions involved in actinide transport is instrumental in managing human contamination. Here we show that siderocalin, a mammalian siderophore-binding protein from the lipocalin family, specifically binds lanthanide and actinide complexes through molecular recognition of the ligands chelating the metal ions. Using crystallography, we structurally characterized the resulting siderocalin–transuranic actinide complexes, providing unprecedented insights into the biological coordination of heavy radioelements. In controlled in vitro assays, we found that intracellular plutonium uptake can occur through siderocalin-mediated endocytosis. We also demonstrated that siderocalin can act as a synergistic antenna to sensitize the luminescence of trivalent lanthanide and actinide ions in ternary protein–ligand complexes, dramatically increasing the brightness and efficiency of intramolecular energy transfer processes that give rise to metal luminescence. Our results identify siderocalin as a potential player in the biological trafficking of *f* elements, but through a secondary ligand-based metal sequestration mechanism. Beyond elucidating contamination pathways, this work is a starting point for the design of two-stage biomimetic platforms for photoluminescence, separation, and transport applications.

actinide transport | siderocalin | protein crystallography | luminescence spectroscopy | antenna effect

Events of the last decade have heightened public concern that radionuclides may be released to the environment either deliberately or accidentally (1, 2), with such events potentially leading to the internal contamination of a large number of individuals. The actinides are all highly radioactive, as are some lanthanide fission products, and many of their isotopes decay by alpha particle emission (3). Once internalized, they are distributed to various tissues with patterns that depend on the chemical and physical form of the contaminant in question (4). The densely ionizing alpha particles emitted by actinides when retained can cause tissue damage and induce cancer in target tissues in a dose-dependent manner (5). Sufficiently high radionuclide doses may also cause manifestations of acute radiation syndrome. The tissue distribution of an actinide will therefore determine the pattern of injury observed and its radiological and chemical toxicities may lead to serious adverse health effects (6–8). Although they are known to rapidly circulate and deposit into major organs such as bone, liver, or kidney after contamination (6, 8–10), the specific molecular mechanisms associated with mammalian uptake of these toxic heavy elements remain largely unexplored. Proposed mammalian actinide acquisition and transport mechanisms have typically focused on proteins that use conserved motifs to directly bind the essential elements iron or calcium (6, 8, 10–13), such as transferrin (14–18), ferritin (13), osteopontin (19), or fetuin (20). Siderocalin (Scn), an essential antibacterial protein that sequesters iron (21, 22), and an important component of iron trafficking (23), is distinct in that it binds ferric iron indirectly, through tight complexes with a siderophore or siderophore-derived chelator. For example, Scn binds the archetypical hexadentate siderophore Enterobactin (Ent; Fig. 1*A*) as a ferric complex ($[Fe^{III}(Ent)]^{3-}$) with a subnanomolar equilibrium dissociation constant (K_d = 0.4 nM) (22). The binding of $[Fe^{III}(Ent)]^{3-}$ by Scn is mainly driven by electrostatic and cation-π interactions with the three Ent catecholamide moieties (22) (Fig. 1*B*), rather than the metal directly, allowing other metals to be substituted (24) (e.g., Al, Ga, V, and In), with some metal–Ent complexes showing even tighter binding than $[Fe^{III}(Ent)]^{3-}$. We hypothesized that the metal ion could be further substituted without affecting recognition significantly, potentially uncovering endogenous trafficking pathways for other elements or enabling novel applications. We therefore investigated the affinity of Scn for lanthanide and actinide complexes of Ent and of the synthetic octadentate hydroxypyridinonate siderophore analog, 3,4,3-LI(1,2-HOPO) ("HOPO"; Fig. 1*A*), reported to form some of the most stable, fully coordinated *f*-element complexes (25, 26). Further X-ray diffraction and spectroscopic characterization of the resulting Scn adducts formed with chelated *f* elements provided crystal structures of protein complexes with four actinide elements (Th, Pu, Am, and Cm), and revealed the protein as an antenna that sensitizes metal luminescence through highly efficient intramolecular energy transfer processes. Finally, the potential role of Scn in actinide transport was examined through a series of in vitro experiments probing the cellular uptake of plutonium. The two-stage protein–ligand-based metal sequestration mechanism described here therefore paves the way to new avenues not only in exploring the biological chemistry of actinide

Significance

The release of actinides in the environment, particularly after a nuclear power plant accident or the potential use of a radiological dispersal device, is a public health threat, as all actinides are radioactive and will trigger damage once internalized by the human body. The biological chemistry of actinide metal ions is largely unknown and new approaches to the understanding of pathways underlying contamination are needed. This work identifies a new mammalian pathway for the intracellular delivery of the radioactive toxic metal ions that are actinides, through the protein siderocalin. Spectroscopic tools, including X-ray diffraction and luminescence, provided insights on the coordination of these metal ions, which is crucial to devise new strategies for decontamination.

Author contributions: B.E.A., P.B.R., S.S.G., D.D.A., R.K.S., and R.J.A. designed research; B.E.A., P.B.R., S.S.G., D.D.A., C.Y.R., and M.S.-H. performed research; B.E.A., P.B.R., S.S.G., D.D.A., C.Y.R., M.S.-H., R.K.S., and R.J.A. analyzed data; and B.E.A., P.B.R., R.K.S., and R.J.A. wrote the paper.

The authors declare no conflict of interest.

This article is a PNAS Direct Submission.

Data deposition: Crystallographic, atomic coordinates, and structure factors were deposited in Protein Data Bank (accession codes: 4ZFX, 4ZHC, 4ZHD, 4ZHF, 4ZHG, and 4ZHH).

[1]To whom correspondence should be addressed. Email: rjabergel@lbl.gov.

This article contains supporting information online at www.pnas.org/lookup/suppl/doi:10.1073/pnas.1508902112/-/DCSupplemental.

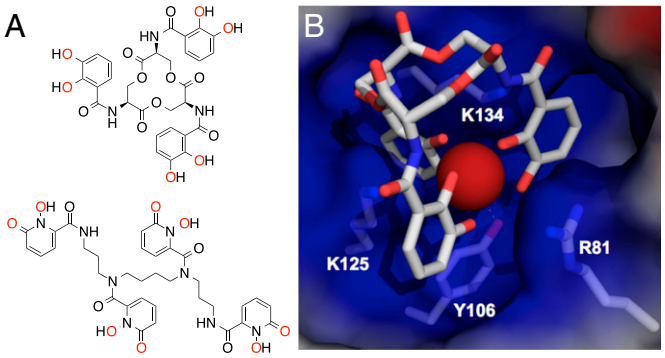

Fig. 1. Determination of Scn affinity for Ent and 3,4,3-LI(1,2-HOPO) complexes of selected lanthanide and actinide elements. (*A*) Molecular structures of the hexadentate Ent (*Upper*) and octadentate 3,4,3-LI(1,2-HOPO) (HOPO; *Lower*) ligands; metal-binding atoms are shown in red. (*B*) A view into the Scn calyx, showing the interaction between key residue side chains and $[Fe^{III}(Ent)]^{3-}$. Scn is shown as a semitransparent molecular surface, colored by electrostatic potential (blue = positive, red = negative). Side chains are labeled and shown in a licorice-stick representation, colored by atom type (carbon: gray, nitrogen: blue, and oxygen: red). A direct contact between Y106 and the iron atom (red sphere) is indicated with a dotted line. The snugness of the K125/K134 "key" pocket is apparent, as is the steric occlusion of adducts to the 3, 4, and 5 positions of the catechol bound there. The deepest calyx pocket is at the upper right.

contamination but also in designing future separation and photoluminescence tools.

Results and Discussion

High Affinity of Scn for *f*-Element Complexes. The affinity of Scn for an apo- or holo-siderophore can be quantified by monitoring the intrinsic fluorescence of the protein upon siderophore-binding (22, 24). The equilibrium dissociation constants (K_d) of Scn for various metal complexes with Ent ($[M^{III}(Ent)]^{3-}$, M^{III} = Sm, Eu, Gd, ^{243}Am, or ^{248}Cm, or $[M^{IV}(Ent)]^{2-}$, M^{IV} = Th or ^{242}Pu), or with HOPO ($[M^{III}(HOPO)]^{-}$ or $[M^{IV}(HOPO)]$) were determined (Table 1). In general, Scn bound metal–HOPO complexes with weaker affinities than the corresponding Ent complexes, and affinity decreased with the overall anionic charge of the metal complexes, consistent with a recognition mechanism dominated by cation-π and electrostatic interactions. However, some subtleties were observed in the recognition patterns. Analysis of the data also showed similar K_d values to $[Fe^{III}(Ent)]^{3-}$ for the similarly charged $^{243}Am^{III}$ and $^{248}Cm^{III}$ Ent complexes, but weaker binding values were observed for the corresponding lanthanide complexes. Such discrimination between 4*f*- and 5*f*-element complexes with formal +3 metal oxidation state is of particular interest for the probing of *f*-orbital bonding differences, a key aspect of separation method development in nuclear fuel process applications. Another peculiarity to be noted is the remarkably strong Scn binding of the $[Pu^{IV}(Ent)]^{2-}$ complex, one order of magnitude stronger than that of $[Th^{IV}(Ent)]^{2-}$, despite its lesser anionic charge compared with $[Fe^{III}(Ent)]^{3-}$.

Structural Characterization of Scn Adducts. The general recognition mechanism of Scn has been extensively studied and is well understood (22, 24, 27–33). Ligands bind in the highly sculpted protein calyx, where the key interaction is through an aryl group binding in a snug pocket between the side chains of K125 and K134, with electrostatic and cation-π interactions to this ring and neighboring ones mediated by the side chains of R81, K124, and K134 (Fig. 1*B*). In various complexes, the side chain of W79 swaps position for R81, making alternate ring–ring interactions with catecholate groups or stacking interactions with noncatecholate groups. The deepest pocket in the calyx, unoccupied (except for an ordered water molecule or ion) in most of the catecholate ligand structures, is specific for the terminal carboxylate group of an extended acyl chain in the largest known natural Scn ligands, the soluble carboxymycobactin (CMB) siderophores of mycobacteria (34). The Y106 hydroxyl is positioned to also contribute direct polar contacts to a chelated metal, and overall calyx/ligand shape complementarity provides additional van der Waals contacts (Fig. 1*B*).

To confirm specific binding, reveal the details of protein–ligand and chelator–metal coordination, and highlight differences in the recognition of nontransition metals with natural or synthetic chelators, Scn was cocrystallized with $[Th^{IV}(Ent)]^{2-}$, $[Th^{IV}(TRENCAM)]^{2-}$ (a synthetic analog of Ent; ref. 24), $[Pu^{IV}(Ent)]^{2-}$, and the Sm, Eu, Gd, ^{243}Am, or ^{248}Cm $[M^{III}(HOPO)]^{-}$ complexes. Six cocrystal structures were successfully determined (Fig. 2 *A–F* and *SI Appendix*, Table S1), all of which clearly showed the presence of metal and chelator, confirming specific binding. The catecholate–Th and catecholate–Pu structures (Fig. 2 *A–C*) show clear electron density for the metal, but the only part of the hexadentate chelator that was resolvable is the catechol moiety binding in the K125/K134 pocket. Prior structural analyses had shown that $[Fe^{III}(Ent)]^{3-}$ is susceptible to backbone hydrolysis in the Scn calyx (27), but TRENCAM is nonhydrolyzable, so partial disordering of Ent or TRENCAM in these structures is likely accounted for by a combination of the inability of these tightly constrained chelators to fully coordinate ions larger than Fe^{3+}, and the inability of the tightly constrained calyx to accommodate equatorial expansion of the metal–chelator complex. This latter property is consistent with the inability of Scn to accommodate salicylate-mode binding ferric siderophores (27), and explains the observation of an uncoordinated catechol group in the $[Th^{IV}(TRENCAM)]^{2-}$ complex structure (Fig. 2*B*). The Sm, ^{243}Am, and ^{248}Cm $[M^{III}(HOPO)]^{-}$ complexes, on the other hand, showed clear density for the entire chelator, all of which are essentially identical in structure (Fig. 2 *D–F*). The octadentate HOPO coordination around the metal centers adopted a nonstandard, "snub disphenoid" geometry (Fig. 2*G*).

To understand how the structure of Scn adjusts in binding a wide range of ligands, we superimposed 73 individual views of Scn alone, or bound to natural or synthetic ligands (Fig. 2 *H–J*). This analysis revealed remarkable structural rigidity: overall backbone structure, α-carbon atoms positions of calyx-lining residues, and even most of the ligand-contacting side-chain rotamers are essentially absolutely conserved across this entire comparison set. The only structural elements that respond to divergent ligands are the side chains of W79 and R81, and, to a much lesser degree, Y106 and K125. R81 occupies multiple conformers, with extremes ranging from nearly pushed out of the calyx to accommodate the large CMB ligands (highlight 1 in Fig. 2*I*), to intercalating between catechols in Ent-like siderophores, providing cation-π interactions (as in Fig. 1*B* and highlight 2 in Fig. 2*I*). K125 adopts a single conformation in almost all Scn structures, except in the $[M^{III}(HOPO)]^{-}$ structures, where it moves outward slightly, by almost 2 Å at Nζ, to accommodate the fourth hydroxypyridinone group within the calyx (highlight 3 in Fig. 2*I*). W79 moves through a range of

Table 1. Scn-binding constants calculated from fluorescence quenching analyses with different metal complexes at pH 7.4

Ent Complex	K_d, nM (SD)	HOPO complex	K_d, nM (SD)
$[Fe^{III}(Ent)]^{3-}$	0.4 (ref. 22)		
$[Sm^{III}(Ent)]^{3-}$	7(2)	$[Sm^{III}(HOPO)]^{-}$	13(3)
$[Eu^{III}(Ent)]^{3-}$	8(2)	$[Eu^{III}(HOPO)]^{-}$	14(1)
$[Gd^{III}(Ent)]^{3-}$	5.4(4)	$[Gd^{III}(HOPO)]^{-}$	18(2)
$[Th^{IV}(Ent)]^{2-}$	13(5)	$[Th^{IV}(HOPO)]$	no binding
$[Pu^{IV}(Ent)]^{2-}$	0.09(1)	$[Pu^{IV}(HOPO)]$	110(21)
$[Am^{III}(Ent)]^{3-}$	0.24(5)	$[Am^{III}(HOPO)]^{-}$	29(1)
$[Cm^{III}(Ent)]^{3-}$	0.20(9)	$[Cm^{III}(HOPO)]^{-}$	22(5)

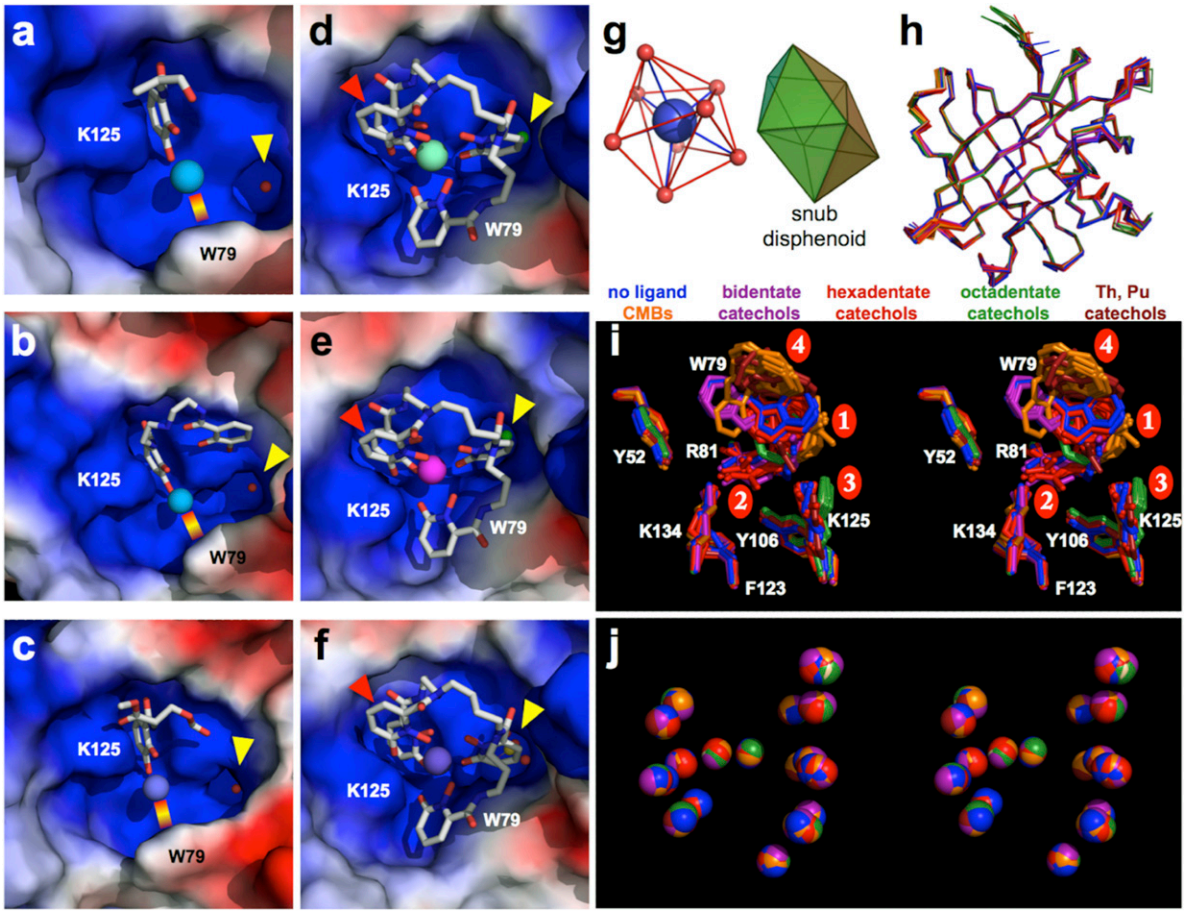

Fig. 2. Crystallographic analyses of the binding of chelated lanthanides and actinides by Scn. Views into the Scn calyx for the complexes with (*A*) $[Th^{IV}(Ent)]^{2-}$; (*B*) $[Th^{IV}(TRENCAM)]^{2-}$ (a synthetic analog of Ent; ref. 24); (*C*) $[Pu^{IV}(Ent)]^{2-}$; (*D*) $[Sm^{III}(HOPO)]^{-}$; (*E*) $[^{243}Am^{III}(HOPO)]^{-}$; and (*F*) $[^{248}Cm^{III}(HOPO)]^{-}$. The protein is shown in a molecular surface representation, colored by electrostatic potential (red = negative, blue = positive), the chelating group is shown in a licorice-stick representation, colored by atom type (carbon: gray, nitrogen: blue, and oxygen: red), and the metal is shown as a colored sphere. Ordered water molecules or ions (chloride: green, and sulfate: yellow/red) bound in the deepest calyx pocket are indicated by the yellow arrows; red arrows highlight the position of the fourth hydroxypyridinone group of the HOPO chelators (*D*, *E*, and *F*). The positions of the side chains of key calyx residues (K125, W79) are indicated, as are the positions of presumed cation-π interactions (gradient bars in *A*, *B*, and *C*). (*G*) The coordination of Sm, ^{243}Am, and ^{248}Cm in the HOPO complexes is shown as a network of isolated HOPO hydroxyl oxygen atoms (red balls) around the metal (blue sphere) on the left, compared with a snub disphenoid geometric solid on the right. (*H*) The carbon-α backbones of 73 Scn molecules from available crystal structures (the structures described in this work plus PDB (41) accession codes 1DFV, 1L6M, 1 × 71, 1 × 89, 1 × 8U, 3FW4, 3FW5, 3HWE, 3HWF, 3HWG, 3K3L, 3PEC, 3PED, 3TF6, 3TZS, 3UOD, and 4K19) are superimposed; there are up to six Scn molecules per asymmetric unit in the various structures. These structures are colored by the type of ligand bound, as indicated. This view is rotated about 120° anticlockwise around the normal to the page from that in *A*–*F*. (*I*) A stereoview of the side chains of key calyx residues, colored as in *H*, isolated from the 73-structure superposition. Key positions discussed in the text are numbered. (*J*) A stereoview of the isolated carbon-α atoms of from all residues with an atom within 4 Å of any ligand from the 73-molecule superposition shows almost no concerted flexing of the calyx, widening or narrowing, in response to binding any type of ligand.

rotamers, most dramatically shifting to optimize binding to various classes of ligands (highlight 4 in Fig. 2*I*). In the calyx-filling CMB structures and the Th/Pu–hexadentate chelator complexes, W79 adopts a rotamer that points it farthest outward from the calyx. In the CMB structures, this rotamer sterically accommodates these large ligands, but, remarkably, in the Th/Pu structures, this rotamer selection potentially enables a direct cation-π interaction to the partially exposed metal (Fig. 2 *A*–*C*), compensating for their incomplete coordination. In the HOPO complexes, W79 uniformly adopts a disfavored rotamer, not previously observed, pointing downward into the calyx (the green edge just apparent above R81 in Fig. 2*I*), to sterically accommodate the awkward, octadentate HOPO complexes; R81 coordinately adopts an extreme conformation, pushed down against the floor of the calyx. The distorted coordination geometry of the HOPO complexes is thus likely also a consequence of these compounds binding in a confined, inflexible volume. Y106 moves slightly upwards (~1 Å at the hydroxyl), to better engage the metals in the HOPO complexes. An ordered water molecule was found in complexes with −3 charged complexes that fail to fully occupy the calyx (as in Fig. 2 *A*–*C*), or negatively charged counterions (e.g., chloride, sulfate) for the less negatively charged, but more calyx-filling HOPO complexes (as in Fig. 2 *D*–*F*). Scn is thus revealed to be an amazing molecular machine, capable of specific, tight binding to a wide range of ligated metal complexes, using an almost completely rigid binding site with the absolute minimum of moving parts.

Scn-Mediated Pu Uptake in Cells. Incorporation of exogenous metal ions or ligands within the protein calyx did not affect the overall structure of the protein, suggesting that Scn might shuttle *f*-element complexes following an endocytosis pathway similar to that described in the trafficking of ferric ion by the Scn-catechol and Scn-Ent adducts (30). To test this hypothesis, we added the radioactive Scn-$[^{238}Pu(Ent)]$ complex to kidney proximal tubule

LLCPK cells and demonstrated ^{238}Pu uptake over a time course of 8 h (Fig. 3*A*). Intracellular accumulation of ^{238}Pu was blocked at 4 °C as expected for active uptake through receptor-mediated endocytosis (30) (average ^{238}Pu content per 10^5 cells of 12 ± 3 pg at 37 °C versus 0.7 ± 0.1 pg at 4 °C, $^{****}P < 10^{-4}$). Cellular ^{238}Pu uptake (8 ± 2 pg per 10^5 cells at 6 h) was curtailed when cells were incubated with Scn-[^{238}Pu(Ent)] in the presence of tenfold excess Scn or Scn-[Fe(Ent)] to 1.9 ± 0.8 and 2.2 ± 0.9 pg per 10^5 cells ($^{***}P < 10^{-3}$), respectively (Fig. 3*B*). This sharp reduction is consistent with competitive uptake inhibition and indicated that Scn-[^{238}Pu(Ent)] entered the cell through the same receptor-mediated pathway. Finally, dose dependence of ^{238}Pu cellular incorporation was demonstrated by incubation of the cells in the presence of 5 and 0.1 nM of Scn-[^{238}Pu(Ent)] over 6 h, which resulted in gradually decreasing cellular content (8- and 1310-fold, respectively, $^{***}P < 10^{-3}$), compared with a 50-nM exposure concentration (Fig. 3*C*). Taken together, these data support the model that Scn mediates cellular ^{238}Pu trafficking and delivery.

Scn-Enhanced Eu and Cm Luminescence Sensitization. We sought to explore the effect of Scn binding on the previously reported remarkable ability of the 3,4,3-LI(1,2-HOPO) ligand to sensitize Eu(III) and Cm(III) luminescence (26, 35) by comparing the photophysical properties of free versus Scn-bound [Eu^{III}(HOPO)]$^-$ and [Cm^{III}(HOPO)]$^-$ (Fig. 4). The electronic absorption spectra of the Scn adducts display the expected absorption maxima due to the protein aromatic amino acids tryptophan (Trp) and tyrosine (Tyr) absorbance at λ_{max} = 278 nm and to the ligand π–π^* transitions at λ_{max} = 320 nm. However, the latter transition is slightly red shifted in comparison with the free complexes (315 nm), an effect of the strong cation-π interactions between the metal complexes and the protein calyx. This decrease of the metal complex singlet excited state observed by UV-visible absorption spectroscopy in the protein adducts is in line with a decreased triplet excited-state energy (~280 cm^{-1} corresponding to a redshift of 4 nm; *SI Appendix*, Fig. S1). The resulting energy gap between the lowest T_1 state of the ligand and the accepting states of the metals is therefore reduced upon binding to Scn, implying that energy transfer processes may be more efficient within the protein environment. Excitation at 325 nm of Scn:[Eu^{III}(HOPO)]$^-$ and Scn:[Cm^{III}(HOPO)]$^-$ yielded characteristic luminescence spectra with very intense emission peaks corresponding to the $^5D_0 \rightarrow {}^7F_2$ and $^6D_{7/2} \rightarrow {}^8S_{7/2}$ hypersensitive transitions of Eu(III) and Cm(III), respectively (Fig. 4 *A* and *B*; *SI Appendix*, Fig. S2). Although luminescence quantum yields of the Scn adducts are comparable to those of the free complexes in solution (20% vs. 16% for Eu and 47% vs. 45% for Cm), protein binding results in a 1.3-fold increase in luminescence brightness for both, and 1.4- and 2.8-fold increases in energy transfer efficiency for the Eu and Cm complexes, respectively (Table 2). More importantly, excitation at 280 nm of the metal complexes and corresponding protein ternary systems revealed a much higher energy transfer enhancement, with 5.3- and 3.7-fold increases in luminescence brightness, and 18.3- and 29.5-fold increases in energy transfer efficiency, for the Eu and Cm complexes, respectively, upon formation of the protein adducts. Although time-resolved analysis revealed similar lifetimes for the free and protein-bound complexes, indicating little change

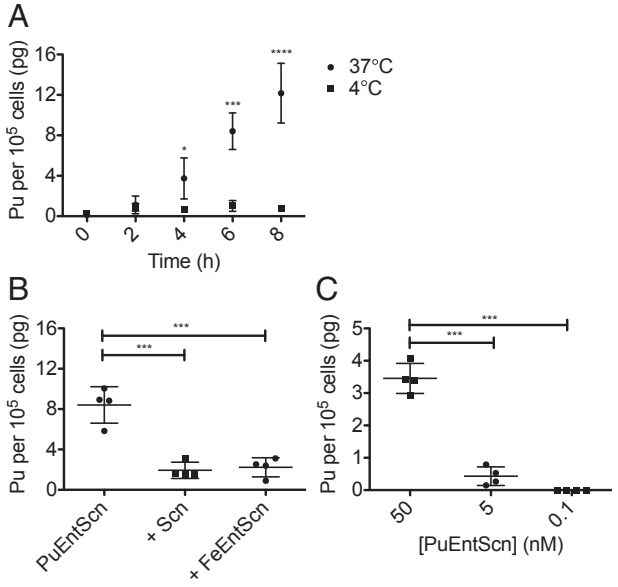

Fig. 3. Cellular uptake of plutonium through Scn-[^{238}Pu(Ent)]. (*A*) Capture of ^{238}Pu from the Scn-[^{238}Pu(Ent)] complex by kidney proximal tubule LLCPK cells in vitro at 37 °C; uptake was inhibited at 4 °C. (*B*) Cellular ^{238}Pu uptake was inhibited upon addition of 10 equivalents of Scn or Scn-[Fe(Ent)] to Scn-[^{238}Pu(Ent)] in the growth medium. (*C*) Cellular incorporation of ^{238}Pu was dependent on the Scn-[^{238}Pu(Ent)] incubation dose. All data represent mean ±SD, n = 4 independent experiments, and statistical significance ($^{***}P < 10^{-3}$; $^{****}P < 10^{-4}$) was assessed by two-tailed Student's t test.

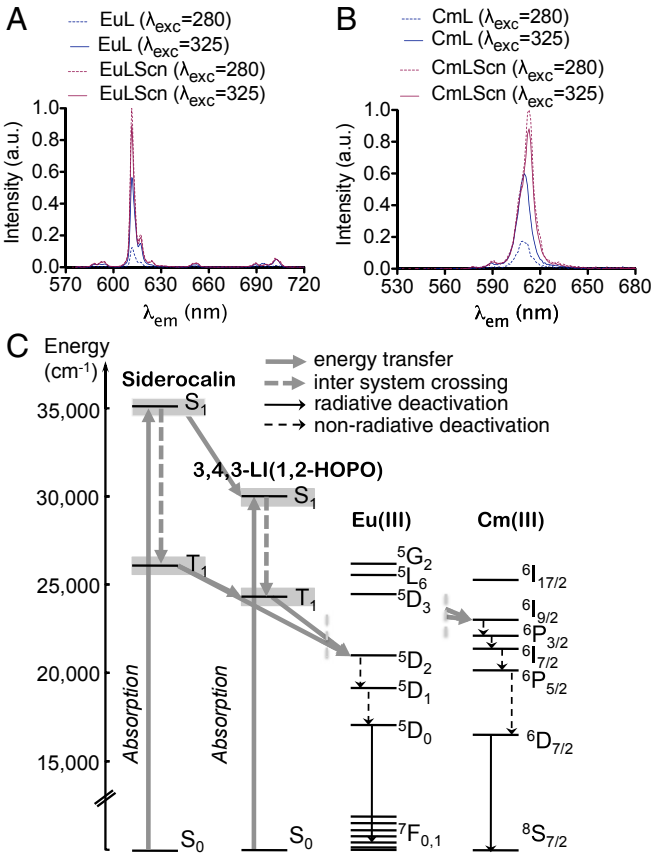

Fig. 4. Synergistically enhanced luminescence sensitization in the Siderocalin-HOPO Eu(III) and Cm(III) complexes. Luminescence spectra of (*A*) free and Scn-bound [Eu^{III}(HOPO)]$^-$ (10 μM, 10 μg/mL ubiquitin, 0.1 M Hepes, pH 7.4) and (*B*) [Cm^{III}(HOPO)]$^-$ (1 μM, 10 μg/mL ubiquitin, 0.1 M Hepes, pH 7.4) after excitation at 280 or 325 nm, showing the enhanced sensitization upon protein binding. All intensities were multiplied by the normalization factor applied to the most intense spectra obtained from the corresponding Scn-bound samples excited at 280 nm. (*C*) Jablonski diagram depicting the synergistic antenna effect in the Eu and Cm protein–ligand–metal complexes.

Table 2. Summary of photophysical parameters determined for free and Scn-bound $[Eu^{III}(HOPO)]^-$ and $[Cm^{III}(HOPO)]^-$

	[Eu(HOPO)]		Scn-[Eu(HOPO)]		[Cm(HOPO)]		Scn-[Cm(HOPO)]	
λ_{exc} (nm)	280	325	280	325	280	325	280	325
ε ($M^{-1}cm^{-1}$)	7,550	16,120	32,880	16,920	8,990	10,790	36,640	13,810
τ_{obs} {H_2O} (ms)	—	0.81(8)	0.92(9)	0.93(9)	—	0.38(4)	0.38(4)	0.39(4)
τ_{calc} {D_2O} (ms)	—	1.15(12)	1.11(11)	1.11(11)	—	0.49(5)	0.43(4)	0.43(4)
Φ_{tot} (H_2O)	0.09(1)	0.16(2)	0.11(1)	0.20(2)	0.19(2)	0.45(5)	0.17(2)	0.47(5)
q	—	0.1(1)	−0.1(1)	−0.2(1)	—	1.1(1)	1.1(1)	1.1(1)
Brightness (M^{-1} cm^{-1})	0.7(1)	2.6(1)	3.7(1)	3.3(1)	1.7(1)	4.9(1)	6.3(1)	6.5(1)
Ratio E_{ScnML}/E_{ML}	—	—	18.3	1.4	—	—	29.5	2.8

Uncertainties determined from the SD between at least three independent experiments in aqueous buffered solutions (pH 7.4).

in metal inner sphere hydration, subtle but significant changes were observed in the emission spectra highlighting the geometry constraints imposed by the protein calyx upon binding (*SI Appendix*, Fig. S3–S5 and Table S2). This unrivaled enhanced emission behavior displayed by the protein adducts can therefore be attributed to a remarkable synergistic energy transfer (36) with the protein and ligand both acting as antennae (Fig. 4*C*). Further studies will probe the kinetics of the possible energy transfer pathways to quantify their respective contribution to the overall sensitization process.

Conclusion

The Scn-mediated metal uptake pathway appears as a previously unidentified target for preventing actinide incorporation and subsequent cellular damage. The design of new strategies for minimizing the deleterious health effects of actinide contamination will however necessitate a better understanding of the interactions between cellular membrane receptors and metal adducts of Scn. Beyond identifying Scn as a potential player in the physiological transport of actinides, and revealing remarkable aspects of the protein's interactions with chelated metals, these results also highlight new potential uses of Scn in applications ranging from the design of photoluminescent materials to the separation of *f* elements in the nuclear fuel process. Finally, potential medical applications also include the functionalization of targeting biologics, for imaging and therapeutic radionuclide delivery, by enabling the selective and stoichiometric chelation of a wide range of elements.

Materials and Methods

Caution. The ^{232}Th, ^{238}Pu, ^{242}Pu, ^{243}Am, and ^{248}Cm are hazardous radionuclides with high specific activities that should only be manipulated in specifically designated facilities, in accordance with appropriate safety controls.

General Considerations. Chemicals were obtained from commercial suppliers and were used as received. Ent was provided by Prof. K. N. Raymond (University of California, Berkeley). The ligand 3,4,3-LI(1,2-HOPO) was prepared and characterized as previously described (37). The $LnCl_3{\cdot}nH_2O$ lanthanide salts used were of the highest purity available (>99.9%). A stock solution of $^{232}Th(IV)$ was prepared from $^{232}ThCl_4{\cdot}8H_2O$ (Baker & Adamson), and a stock of $^{238}Pu(IV)$ was purchased as $^{238}Pu(NO_3)_4$ in 4 M HNO_3 from Eckert & Ziegler (lot 118521). The ^{242}Pu was received from Oak Ridge National Laboratory as PuO_2 (lot Pu-242–327 A, 99.93 wt% of metal ^{242}Pu) and a stock solution of $^{242}Pu(IV)$ was prepared as described previously (38). The ^{242}Pu isotope was used for spectroscopic experiments whereas ^{238}Pu was used in cellular uptake studies. Aliquots of acidified stocks of carrier-free ^{243}Am and ^{248}Cm (95.78% ^{248}Cm, 4.12% ^{246}Cm, 0.06% ^{245}Cm, 0.02% $^{244}Cm/^{247}Cm$ isotopic distribution by atom percentage) from the Lawrence Berkeley National Laboratory were used. All solutions were prepared using deionized water purified by a Millipore Milli-Q reverse osmosis cartridge system, and pH was adjusted with concentrated HCl or NaOH when needed. All thermodynamic and spectroscopic measurements were conducted at room temperature.

Metal, Ligand, and Protein Working Solutions. The metal working stock solutions were prepared in standardized 0.1 M HCl. Ligand stock solutions (4 mM) were prepared by direct dissolution of a weighed portion of ligand in DMSO. Recombinant human Scn was prepared as previously described (22).

UV-Visible Spectroscopy. Absorption spectra were recorded on a Varian Cary G5 double beam absorption spectrometer or a NanoDrop 2000C, using quartz cells of 1.00-cm path length.

Fluorescence Spectroscopy. Emission spectra were recorded on a HORIBA Jobin Yvon IBH FluoroLog-3 spectrofluorimeter, used in steady state mode and luminescence lifetimes were determined with time-correlated single photon counting and multichannel scaling measurements (details provided in *SI Appendix*). Quantum yields and kinetic parameters were determined as previously described (26, 39). The brightness was calculated as the product of the molar absorption coefficient and the luminescence quantum yield. Energy transfer efficiency ratios were calculated using a method derived by Ghorai et al. (*SI Appendix*) (36).

Fluorescence Quenching Binding Assay. Equimolar amounts of metal and chelator were used to constitute metal–chelator solutions (2 μM, pH 7.4, 5% DMSO) in TBS; the 1:1 stoichiometry of the metal–Ent complexes was verified by the Job's method (*SI Appendix*, Fig. S6). Recombinant wild-type Scn (50 nM, 3 mL, 10 μg/mL ubiquitin, TBS pH 7.4, 5% DMSO) was then titrated with a metal–chelator solution. Fluorescence quenching of Scn was measured after each titrant addition, with 3-nm slit band pass, using the characteristic wavelengths λ_{exc} = 280 and λ_{em} = 320–360 nm. Fluorescence values were corrected for dilution upon addition of titrant. Fluorescence data were analyzed by nonlinear regression analysis of fluorescence response versus ligand concentration using a one-site binding model in the program HypSpec (40). The K_d values (as defined in *SI Appendix*) are the results of at least three independent titrations.

Crystallography. For crystallization, 1 mM solutions of equimolar metal/chelator complexes (prepared as above) were mixed in a 2:1 molar ratio with Scn, which was then buffer exchanged into 25 mM pipes (pH = 7.0), and concentrated to ~10 mg/mL protein. Diffraction-quality crystals were grown by vapor diffusion from drops containing 2 μL of ternary metal–chelator–protein complex plus 2 μL of well solution [50 mM NaCl, 200 mM Li_2SO_4, 100 mM NaOAc (pH = 4.1–4.3), 1.2–1.4 M $(NH_4)_2SO_4$]. Because of the hazardous nature of the radionuclides and the requirement that they be manipulated only at designated facilities, actinide complex crystals were grown on site at the Lawrence Berkeley National Laboratory. Crystals were cryopreserved by transfer to 50 mM NaCl, 200 mM Li_2SO_4, 100 mM NaOAc (pH = 4.1), 1.2 M $(NH_3)_2SO_4$, and 20% vol/vol glycerol. Diffraction data were collected at −160 °C in house on a Rigaku MicroMax-007 HF rotating anode X-ray generator with Varimax HF optics (for the Th–Ent crystal), on beamline 5.0.1 (Th-TRENCAM and Sm crystals), or beamline 5.0.2 (Pu, Am, and Cm crystals) at the Advanced Light Source (ALS). Due to potential contamination, a protective barrier of aluminum foil was constructed around the goniometer, and all actinide complex crystals were hand-mounted. Diffraction data were analyzed as described in the *SI Appendix*. Crystallographic statistics are reported in the *SI Appendix*, Table S1. Final models have been deposited in the PDB (41).

Cellular Uptake Determination. Porcine kidney proximal tubule LLC-PK1 cells (ATCC, CL-101) were cultured as detailed in the *SI Appendix*. For uptake experiments, cells were plated at 10^3 to 10^5 cells/well in 24-well plates (Greiner

Bio-One). After 24 h, the wells were washed twice with Ca^{2+}/Mg^{2+} free DPBS, and serum-free DMEM containing the protein–ligand–metal complexes was added. At each time point the medium was removed from the well and the wells were washed twice with Ca^{2+}/Mg^{2+} free DPBS. The cells were trypsinized, counted with a hemocytometer, and viability was measured by trypan blue exclusion. Viability was 100% for all cells in experiments performed at 37 °C, indicating that the low concentrations of ^{238}Pu used for those uptake assays were nontoxic. A decrease in viability (down to ∼85%) was observed for the last two time points of the experiment performed at 4 °C. Cells were then washed twice with Ca^{2+}/Mg^{2+} free DPBS. The cell pellet was resuspended in 1 mL of Ca^{2+}/Mg^{2+} free DPBS and added to scintillation mixture for radioanalysis by liquid scintillation counting (Packard Tri-Carb model B4430, Perkin-Elmer). For the first two series of experiments (uptake comparison at 37 °C and 4 °C, and uptake inhibition upon addition of 10 equivalents of Scn or Scn-[Fe(Ent)]), cells were incubated with 50 nM Scn-[^{238}Pu(Ent)] in the growth medium. For the third series of uptake experiments probing dose dependence, the concentration of Scn-[^{238}Pu(Ent)] was varied from 50 to 0.1 nM. The ^{238}Pu concentrations were measured by liquid scintillation counting. Each experiment was repeated independently 4 times, and results were expressed as means ± SD, with unpaired two-tailed Student's *t* tests. Statistical analyses were performed using GraphPad Prism 5 (GraphPad Software, Inc.).

ACKNOWLEDGMENTS. We thank Marc Allaire, Simon Morton, Jeffrey Bramble, and Israel Tadesse for assistance in planning and implementing diffraction data collection on radioactive crystals at the ALS 5.0.2 beamline. We thank Anthony D'Aléo for luminescence spectroscopy discussions and Kenneth Raymond for providing us with purified Ent. This work was funded by the Division of Chemical Sciences, Geosciences, and Biosciences, Office of Basic Energy Sciences of the US Department of Energy under Contract DE-AC02-05CH11231 (to R.J.A.), and by the National Institutes of Health under Award R01DK073462 (subcontract to R.K.S.). The Advanced Light Source is supported by the Director, Office of Science, Office of Basic Energy Sciences, of the U.S. Department of Energy under Contract DE-AC02-05CH11231.

1. Cassatt DR, et al. (2008) Medical countermeasures against nuclear threats: Radionuclide decorporation agents. *Radiat Res* 170(4):540–548.
2. Pellmar TC, Rockwell S; Radiological/Nuclear Threat Countermeasures Working Group (2005) Priority list of research areas for radiological nuclear threat countermeasures. *Radiat Res* 163(1):115–123.
3. Katz JJ, Seaborg GT, Morss LR (1986) *The Chemistry of the Actinide Elements* (Chapman and Hall, London, UK), 2nd ed.
4. Taylor DM, Stradling GN, Henge-Napoli MH (2000) The scientific background to decorporation. *Radiat Prot Dosimetry* 87(1):11–17.
5. Paquet F, Frelon S, Cote G, Madic C (2003) The contribution of chemical speciation to internal dosimetry. *Radiat Prot Dosimetry* 105(1-4):179–184.
6. Durbin PW (2006) in *The Chemistry of the Actinide and Transactinide Elements*, eds. Morss LR, Edelstein NM, & Fuger J (Springer, Dordrecht, The Netherlands), pp. 3339-3440.
7. Nesmerak K (2013) *Encyclopedia of Metalloproteins*, eds Kretsinger RH, Uversky VN, Permyakov EA (Springer, New York), pp 1098–1103.
8. Taylor DM (1989) The biodistribution and toxicity of plutonium, americium and neptunium. *Sci Total Environ* 83(3):217–225.
9. Melo DR, Weber W, Doyle-Eisele M, Guilmette RA (2014) Comparison of plutonium systemic distribution in rats and dogs with published data in humans. *Int J Radiat Biol* 90(11):1025–1029.
10. Vidaud C, Bourgeois D, Meyer D (2012) Bone as target organ for metals: The case of f-elements. *Chem Res Toxicol* 25(6):1161–1175.
11. Ansoborlo E, et al. (2006) Actinide speciation in relation to biological processes. *Biochimie* 88(11):1605–1618.
12. Aryal BP, Paunesku T, Woloschak GE, He C, Jensen MP (2012) A proteomic approach to identification of plutonium-binding proteins in mammalian cells. *J Proteomics* 75(5):1505–1514.
13. Taylor DM (1998) The bioinorganic chemistry of actinides in blood. *J Alloys Compd* 271:6–10.
14. Deblonde GJ-P, Sturzbecher-Hoehne M, Mason AB, Abergel RJ (2013) Receptor recognition of transferrin bound to lanthanides and actinides: A discriminating step in cellular acquisition of f-block metals. *Metallomics* 5(6):619–626.
15. Jeanson A, et al. (2010) The role of transferrin in actinide(IV) uptake: Comparison with iron(III). *Chemistry* 16(4):1378–1387.
16. Jensen MP, et al. (2011) An iron-dependent and transferrin-mediated cellular uptake pathway for plutonium. *Nat Chem Biol* 7(8):560–565.
17. Sturzbecher-Hoehne M, Goujon C, Deblonde GJ-P, Mason AB, Abergel RJ (2013) Sensitizing curium luminescence through an antenna protein to investigate biological actinide transport mechanisms. *J Am Chem Soc* 135(7):2676–2683.
18. Vidaud C, et al. (2007) Structural consequences of binding of UO2(2+) to apotransferrin: Can this protein account for entry of uranium into human cells? *Biochemistry* 46(8): 2215–2226.
19. Qi L, et al. (2014) Characterization of UO2(2+) binding to osteopontin, a highly phosphorylated protein: Insights into potential mechanisms of uranyl accumulation in bones. *Metallomics* 6(1):166–176.
20. Basset C, et al. (2013) Revision of the biodistribution of uranyl in serum: Is fetuin-A the major protein target? *Chem Res Toxicol* 26(5):645–653.
21. Flo TH, et al. (2004) Lipocalin 2 mediates an innate immune response to bacterial infection by sequestrating iron. *Nature* 432(7019):917–921.
22. Goetz DH, et al. (2002) The neutrophil lipocalin NGAL is a bacteriostatic agent that interferes with siderophore-mediated iron acquisition. *Mol Cell* 10(5):1033–1043.
23. Chen C, Paw BH (2012) Cellular and mitochondrial iron homeostasis in vertebrates. *Biochim Biophys Acta* 1823(9):1459–1467.
24. Abergel RJ, Moore EG, Strong RK, Raymond KN (2006) Microbial evasion of the immune system: Structural modifications of enterobactin impair siderocalin recognition. *J Am Chem Soc* 128(34):10998–10999.
25. Sturzbecher-Hoehne M, Choi TA, Abergel RJ (2015) Hydroxypyridinonate complex stability of group (IV) metals and tetravalent f-block elements: The key to the next generation of chelating agents for radiopharmaceuticals. *Inorg Chem* 54(7): 3462–3468.
26. Sturzbecher-Hoehne M, Kullgren B, Jarvis EE, An DD, Abergel RJ (2014) Highly luminescent and stable hydroxypyridinonate complexes: A step towards new curium decontamination strategies. *Chemistry* 20(32):9962–9968.
27. Abergel RJ, et al. (2008) The siderocalin/enterobactin interaction: A link between mammalian immunity and bacterial iron transport. *J Am Chem Soc* 130(34): 11524–11534.
28. Abergel RJ, et al. (2006) Anthrax pathogen evades the mammalian immune system through stealth siderophore production. *Proc Natl Acad Sci USA* 103(49): 18499–18503.
29. Allred BE, Correnti C, Clifton MC, Strong RK, Raymond KN (2013) Siderocalin outwits the coordination chemistry of vibriobactin, a siderophore of Vibrio cholerae. *ACS Chem Biol* 8(9):1882–1887.
30. Bao G, et al. (2010) Iron traffics in circulation bound to a siderocalin (Ngal)-catechol complex. *Nat Chem Biol* 6(8):602–609.
31. Correnti C, et al. (2012) Siderocalin/Lcn2/NGAL/24p3 does not drive apoptosis through gentisic acid mediated iron withdrawal in hematopoietic cell lines. *PLoS One* 7(8): e43696.
32. Hoette TM, et al. (2011) Immune interference in Mycobacterium tuberculosis intracellular iron acquisition through siderocalin recognition of carboxymycobactins. *ACS Chem Biol* 6(12):1327–1331.
33. Holmes MA, Paulsene W, Jide X, Ratledge C, Strong RK (2005) Siderocalin (Lcn 2) also binds carboxymycobactins, potentially defending against mycobacterial infections through iron sequestration. *Structure* 13(1):29–41.
34. Lane SJ, Marshall PS, Upton RJ, Ratledge C, Ewing M (1995) Novel extracellular mycobactins, the carboxymycobactins from Mycobacterium avium. *Tetrahedron Lett* 36: 4129–4132.
35. Daumann LJ, et al. (2015) New insights into structure and luminescence of Eu(III) and Sm(III) complexes of the 3,4,3-LI(1,2-HOPO) ligand. *J Am Chem Soc* 137(8):2816–2819.
36. Ghorai SK, Samanta SK, Mukherjee M, Saha Sardar P, Ghosh S (2013) Tuning of "antenna effect" of Eu(III) in ternary systems in aqueous medium through binding with protein. *Inorg Chem* 52(3):1476–1487.
37. Abergel RJ, et al. (2010) Biomimetic actinide chelators: An update on the preclinical development of the orally active hydroxypyridonate decorporation agents 3,4,3-LI (1,2-HOPO) and 5-LIO(Me-3,2-HOPO). *Health Phys* 99(3):401–407.
38. Gorden AEV, et al. (2005) Sequestered plutonium: [Pu(IV)5LIO(Me-3,2-HOPO)2]–the first structurally characterized plutonium hydroxypyridonate complex. *Chemistry* 11(9):2842–2848.
39. Abergel RJ, D'Aléo A, Leung CN, Shuh DK, Raymond KN (2009) Using the antenna effect as a spectroscopic tool: Photophysics and solution thermodynamics of the model luminescent hydroxypyridonate complex [Eu(III)(3,4,3-LI(1,2-HOPO))]-. *Inorg Chem* 48(23):10868–10870.
40. Gans P, Sabatini A, Vacca A (2008) HypSpec (Leeds, UK), Version HypSpec2014.
41. Berman HM, et al. (2000) The Protein Data Bank. *Nucleic Acids Res* 28(1):235–242.